

ABSTRACT

Xue, Xiao. Oriented Liquid Crystalline Polymer Semiconductor Films with Large Ordered Domains. (Under the direction of Dr. Brendan O'Connor).

Organic polymers are potential candidates to replace traditional semiconductor in low cost semiconductor-applications. Charge transport in conjugated polymers has a complex dependence on film morphology. Aligning the polymer chains in the plane of the film simplifies the morphology of the system allowing for insight into the morphological dependence of charge transport in these materials. Here, we demonstrate the in-plane alignment of the liquid crystalline polymer semiconductor poly(2,5-bis(3-tetradecylthiophen-2yl)thieno(3,2-b)thiophene) (pBTTT-C14) using large applied strain while on PDMS and held above its liquid crystal phase transition temperature. This approach represents a novel approach to align liquid crystal polymers. The morphology of the resulting film and charge transport characteristics are analyzed in detail including UV-visible optical spectroscopy, GIXD, AFM and TEM. The level of applied strain is shown to vary the level of in-plane backbone alignment. The strain alignment process is shown to orient that film while maintaining a wide-terraced morphology typically found in spun cast films on low-surface energy substrates. These films significantly contrast previous demonstrations of aligned pBTTT films that show a characteristic ribbon-phase commonly observed in highly aligned pBTTT films produced using other methods such as flow coating. This provides an opportunity to contrast the microstructure between aligned films. The field effect mobility is measured in these films showing that charge mobility increases in the alignment direction and decrease in the transverse direction. Comparing mobility and morphology allows for insight into the grain boundary dependence of charge transport, charge percolation behavior, and structural features that influence the field dependence of charge transport.

© Copyright 2015 by Xiao Xue

All Rights Reserved

Oriented Liquid Crystalline Polymer Semiconductor Films with Large Ordered Domains

by
Xiao Xue

A thesis submitted to the Graduate Faculty of
North Carolina State University
in partial fulfillment of the
requirements for the Degree of
Master of Science

Aerospace Engineering

Raleigh, North Carolina

2015

APPROVED BY:

Dr. Chih-Hao Chang

Dr. Yong Zhu

Dr. Brendan O'Connor
Committee Chair

BIOGRAPHY

Xiao Xue was born April 11, 1986 to Qing Xue and Hong Pan in Anshan, Liaoning, China. He graduated from East China University of Science and Technology and received his BS in Mechanical Engineering in June 2009. He received his MS degree in the same field from Ohio University in June 2013. He received his MS degree in aerospace from North Carolina State University in December 2015.

ACKNOWLEDGMENTS

This research work was supported by the National Science Foundation awards CMMI-1200340 and ECCS-1407885. Low temperature OTFT measurements and contributions to this manuscript by Peter Diemer and Oana D. Jurchescu, were supported by National Science Foundation awards ECCS-1254757 and ECCS-1338012. Portions of this research were carried out at the Stanford Synchrotron Radiation Lightsource, a Directorate of SLAC National Accelerator Laboratory and an Office of Science User Facility operated for the U.S. Department of Energy Office of Science by Stanford University. Thanks for Dr. Joe Kline for the XRD measurement. We thank Michael F. Toney for assistance with the X-ray diffractions measurements. Thanks for Dr. Martin Heeney for the supply of polymer. Thanks for TEM measurement by Dr. Xinran Zhang.

Thank my parents, Qing Xue, Hong Pan, for their support and love throughout my life. I would thank Dr. O'Connor for his patient guidance and help throughout this study.

Thank Dr. Omar Awartani for his help when I first came to this lab.

TABLE OF CONTENTS

| | |
|---|----|
| 1. Introduction | 1 |
| 2. Background | 9 |
| 2.1 pBTTT | 9 |
| 2.2 pBTTT Morphology | 11 |
| 3. Experimental | 13 |
| 3.1 Film Preparation | 13 |
| 3.2 Strain-Align and Transfer | 13 |
| 3.3 Transistor Device Fabrication and Characterization | 16 |
| 3.4 Morphology Characterization | 17 |
| 3.5 Low Temperature OFET Measurement | 18 |
| 4. Result and Discussion | 19 |
| 4.1 UV-Vis Absorbance | 19 |
| 4.2 GIXD | 21 |
| 4.3 AFM | 23 |
| 4.4 TEM | 25 |
| 4.5 Room Temperature Charge Transport Characterization | 31 |
| 4.6 Low Temperature Charge Transport | 36 |
| 4.7 Comparing Charge Transport in Oriented OTFTs with Au and Pt Electrodes ... | 37 |
| 5. Conclusion | 40 |
| 6. References | 32 |

LIST OF FIGURES

| | |
|--|----|
| Figure.1 Schematic of molecules of (CH) _x derivatives | 1 |
| Figure.2 Applications of organic electronics. Top: Organic photovoltaic; Bottom left: OLED TV; Bottom right: Radio Frequency ID(RFID)..... | 2 |
| Figure.3 Comparison of organic electronic and conventional electronic | 3 |
| Figure.4 Organic FET mobility development | 4 |
| Figure.5 one piece of 8-bit microprocessors on flexible plastic foils with 3381 OFETs | 5 |
| Figure.6 schematic of energy level | 5 |
| Figure.7 AFM images of the PCDTPT topography by drop-casting on normal polished Si substrates (without orientation): (A) and (B). and slow-drying on nano-grooved substrates (with orientation): (C) -- (F) | 7 |
| Figure.8 AFM image of the uniaxially oriented film dip-coated at 2μm/s(the scale bar corresponds to 1μm)..... | 8 |
| Figure.9 Schematic illustration of the molecular organization in the thin film deposited at... 10 μm/s in an OFET | 8 |
| Figure.10 Schematic of flow-coating pBTTT | 10 |
| Figure.11 Schematic of rubbing pBTTT | 10 |
| Figure.12 DSC of pBTTT used in this study | 11 |
| Figure.13 AFM images of pBTTT films after flow-coating (a) after casting, (b) terraced morphology, and (c) oriented ribbon shape | 12 |
| Figure.14 The effect of curing time on surface hydrophilization process of PDMS at 80°C | 14 |
| Figure.15 Contact angle of PDMS before and after UV Ozone treatment | 14 |
| Figure.16 Strain and transfer schematic..... | 16 |
| Figure.17 schematic of pBTTT bottom-gate bottom-contact transistor | 17 |
| Figure.18 Absorbance and dichroic ratio vs strain | 21 |
| Figure.19 Schematic of pBTTT backbone alignment..... | 21 |
| Figure.20 GIXD, 2-D image plate data for pBTTT films..... | 23 |
| Figure.21 Tapping-mode AFM images..... | 25 |
| Figure.22 Diffraction patterns and dark field images | 28 |
| Figure.23 TEM color orientation map and diffraction pattern of 0% strained pBTTT film..... | 29 |
| Figure.24 TEM color orientation map and diffraction pattern of 25% strained pBTTT film | 29 |
| Figure.25 TEM color orientation map and diffraction pattern of 50% strained pBTTT film | 30 |
| Figure.26 Mobility vs strain..... | 32 |
| Figure.28 Source-drain current (I _{DS}) for OTFTs..... | 33 |
| Figure.29 The saturated mobility with applied field..... | 34 |
| Figure.30 Channel length dependence (0% and 50% strained) | 35 |
| Figure.31 Channel length dependence (0% and 25% strained) | 36 |

| | |
|---|----|
| Figure.32 Saturated mobility vs temperature. (0% and 50% strained) | 37 |
| Figure.33 Channel length dependence of the saturated mobility for 50% strained films (Au VS Pt)..... | 38 |

1. Introduction

Organic semiconductor was first introduced by Alan J. Heeger, Alan G. MacDiarmid and Hideki Shirakawa. They observed Halogen Derivatives of Polyacetylene(CH)_x was conducting and published this in 1977.^[1] They were awarded Nobel prize for this contribution in 2000.

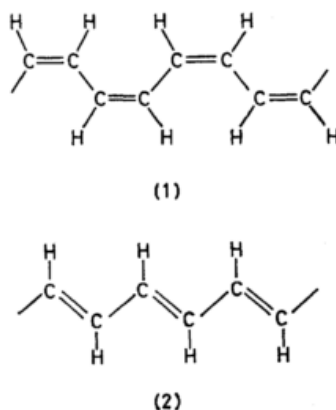


Figure.1 Schematic of molecules of (CH)_x derivatives ^[1]

Organic electronic devices based on organic semiconductor have developed fast recently. Organic electronic have exhibited many advantages over conventional electronics, such as abundant sources, low cost, flexible substrate and large area application. (Figure 3) Nowadays organic electronics are applied to applications such as OLED, OPV and RFID.



Figure.2 Applications of organic electronics. Top: Organic photovoltaic; Bottom left: OLED TV; Bottom right: Radio Frequency ID(RFID)

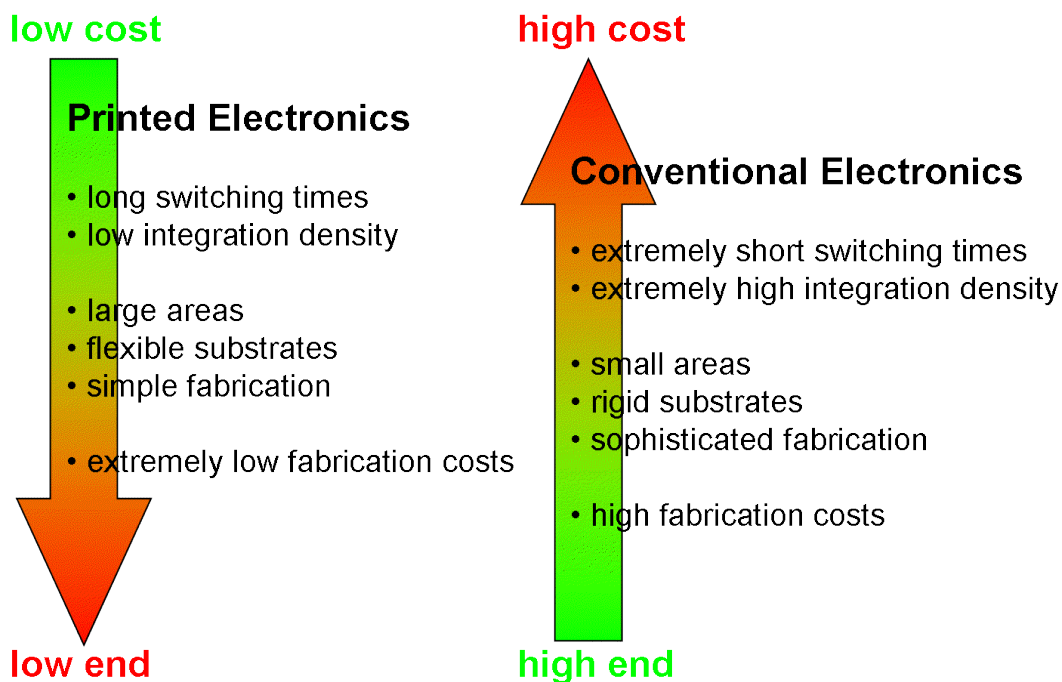


Figure.3 Comparison of organic electronic and conventional electronic^[6]

Organic field effect transistors have attracted research for the past decade due to the potential low cost and flexibility^{[7][8]} in a wide array of applications (**Figure.1**). Organic Field effect transistor was first introduced by Koezuka and co-workers in 1987. The advantage of solution processed organic polymer semiconductor is that they can be processed in simple methods such as spin-cast, drop cast or print at room temperature. This reduces the complicated and costly fabrication process and facilitates many solution based molecular orientation strategies. These strategies has led to further understand of relationship between morphology and electrical properties of organic semiconductor materials. Mobility, the key performance parameter of OFET, has improved to above $1 \text{ cm}^2\text{V}^{-1}\text{s}^{-1}$.^[9,10] This is already comparable to amorphous Si based traditional transistors.^[11]

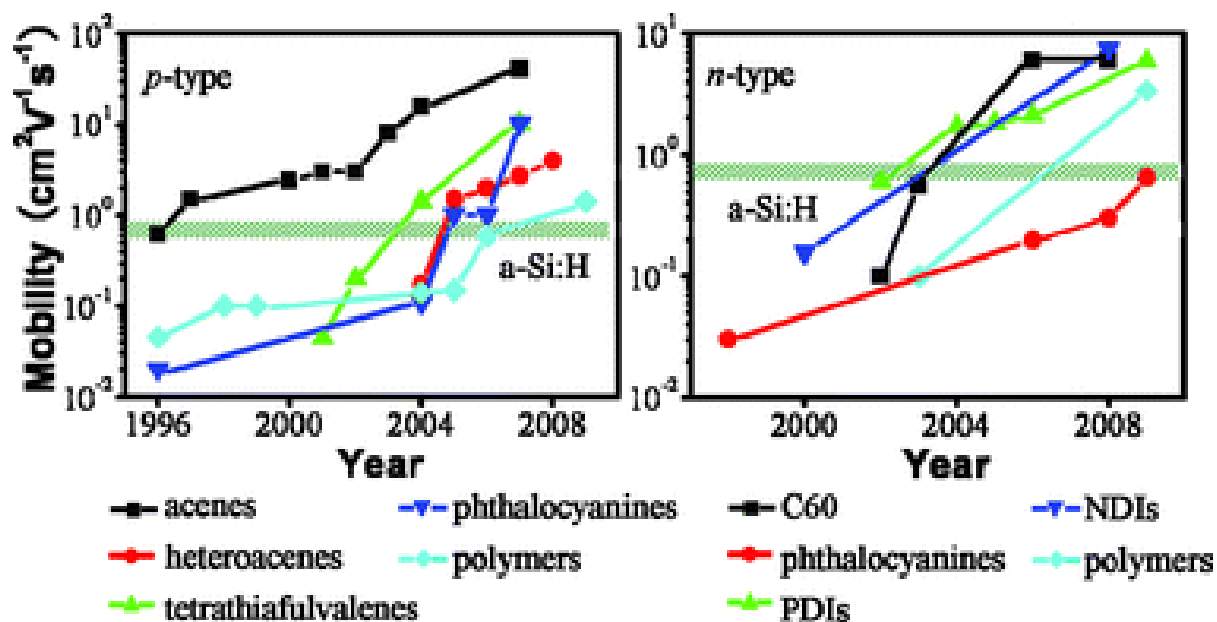


Figure.4 Organic FET mobility development^[12]

In organic field-effect transistors, charge transport is modulated by gate voltage; gate electrode and organic active layer are insulated by gate dielectric layer. In p-type semiconductor based FET, negative voltage is applied on gate, holes begin to accumulate near semiconductor-dielectric interface and transport along the source-drain path in the active layer (**Figure.6**). In p-type OFET, holes travel between source and drain; electrons cannot transport due to the high potential difference between Fermi level and LUMO.

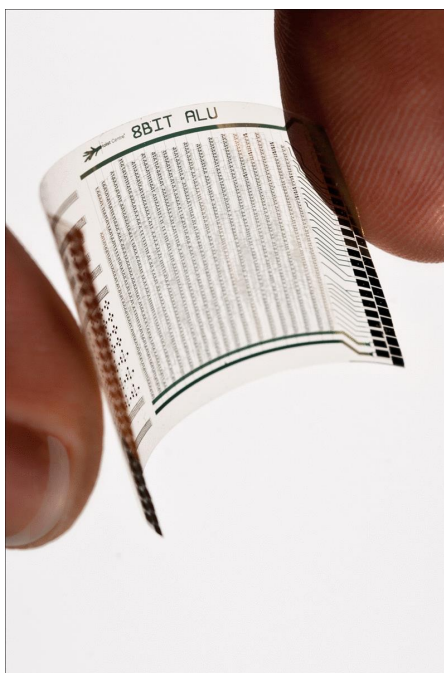


Figure.5 one piece of 8-bit microprocessors on flexible plastic foils with 3381 OFETs ^[13]

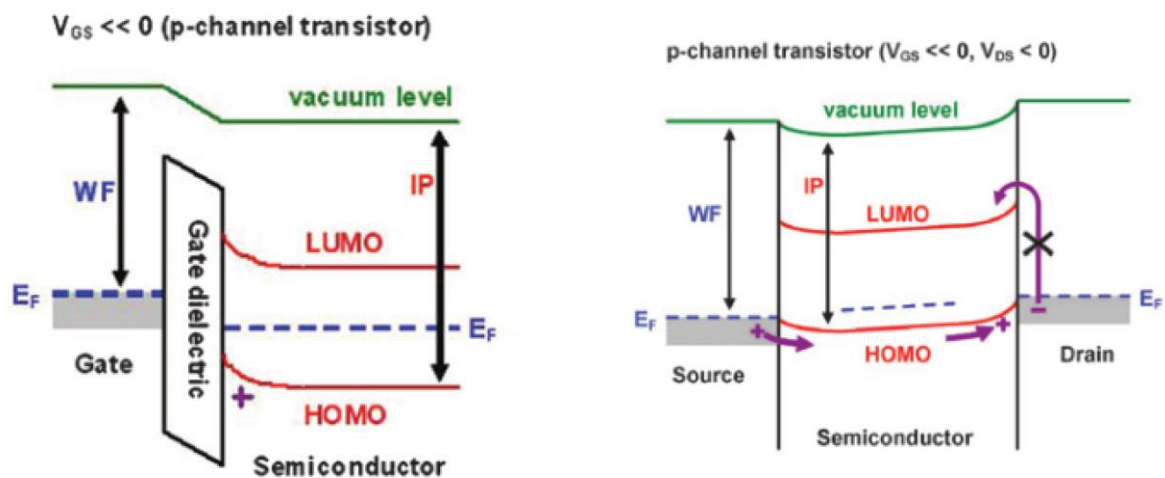


Figure.6 schematic of energy level at semiconductor and dielectric interface(left), schematic of energy level along the source and drain charge transport path(right) ^[14]

Charge transport in organic thin film is closely related to its morphology and processing method.^[15,16] In organic polymer, charge can transport along the backbone, in π - π direction and along side-chain. It is known that along polymer backbone is the most efficient path for charge transport.^[17] Charge transport also happens at intermolecular disordered grain-boundaries. Charge transport is thus a combination of both intramolecular along the backbone and intermolecular in π - π^* stacking direction. In as-cast organic polymer, there is no significant in-plane orientation of molecules, polymer shows general isotropic morphology with no favorable in-plane charge transport direction. This makes it difficult to determine the morphological characteristic that governs charge transport.^[18] In order to gain further insight into polymer morphology and its associated charge transport, aligning strategies have been employed to create anisotropic morphology, such as rubbing,^[19,20] flow-coating,^[21] strain,^[22-25] capillary action,^[26] grooved substrate,^[27,28] shrinking,^[29] embossing^[30] and dip-coating.^[10] The resulted polymer usually shows anisotropic morphology and improved charge mobility in aligned direction.

Alan Heeger and his group employed a nano-groove substrate method to align conjugated copolymer poly[4-(4,4-dihexadecyl-4H-cyclopenta[1,2-b:5,4-b']dithiophen-2-yl)-alt-[1,2,5]thiadiazolo[3,4-c]pyridine] (PCDTPT). (**Figure.7**) Solution is drop cast on grooved substrate and polymer backbone is aligned along the grooved direction.

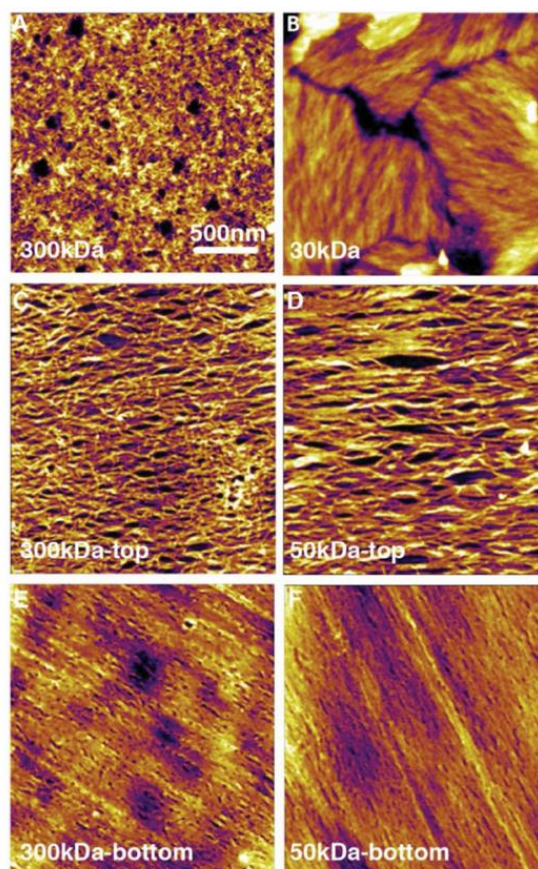


Figure.7 AFM images of the PCDTPT topography by drop-casting on normal polished Si substrates (without orientation): (A) and (B). and slow-drying on nano-grooved substrates (with orientation): (C) -- (F)^[31]

Wang and co-workers have employed solution dip-coating method to align pBTTT on oxide substrate. The level of alignment is controlled by tuning the dip speed. A high mobility of $1.3 \text{ cm}^2\text{V}^{-1}\text{s}^{-1}$ is achieved when dip speed is $2 \mu\text{m/s}$. (**Figure 8-9**)

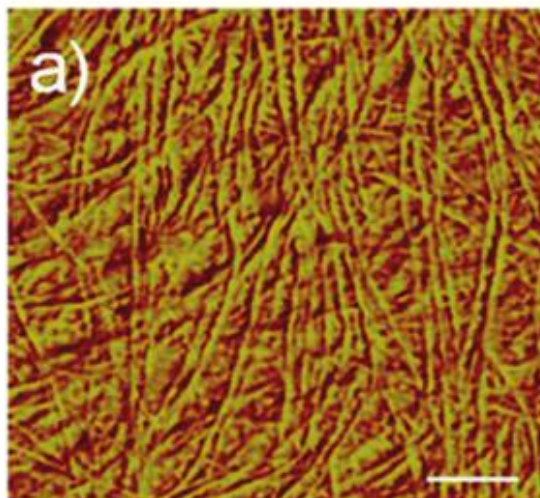


Figure.8 AFM image of the uniaxially oriented film dip-coated at 2 μ m/s(the scale bar corresponds to 1 μ m).^[10]

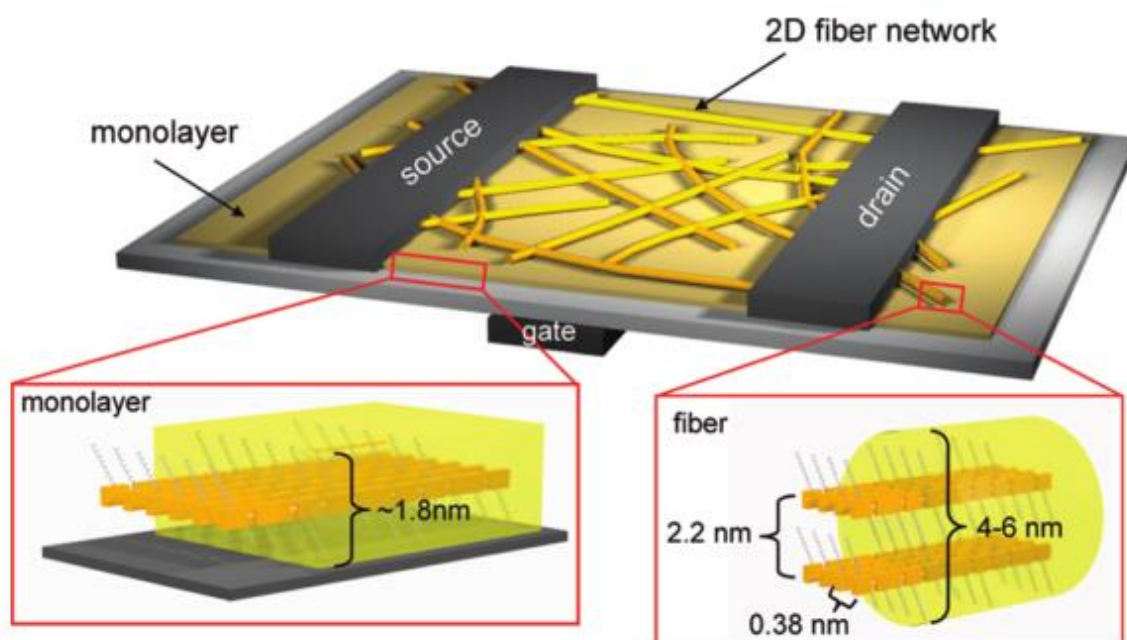


Figure.9 Schematic illustration of the molecular organization in the thin film deposited at 10 μ m/s in an OFET.^[10]

2. Background

2.1 pBTTT

Conjugated liquid crystalline polymer poly(2,5-bis(3-tetradecylthiophen-2yl)thieno(3,2-b)thiophene) (pBTTT-C14) has recently been studied for its highly crystalline and high mobility.^[9,32–39] In order to study the charge transport in pBTTT, people align polymer backbones to achieve anisotropic morphology and charge transport. There are a few effective strategies employed to align pBTTT, such as dip-coating,^[10] flow-coating^[21,36] and high temperature rubbing.^[20] These strategies usually result in highly biaxial orientated films (in-plane alignment and out-of-plane alignment) with significant charge transport anisotropy in along and perpendicular to align directions. Similar to previous research on aligned conjugated polymer.^[22] It is a good opportunity to study grain boundaries after achieving anisotropic morphology and field effect mobility on biaxial orientated conjugated polymer systems since it has been considered to affect charge transport significantly.

Flowing coating employs a moving stage or substrate and injects polymer solution onto substrate. The roller will then rub the as cast solution in order to effectively orientate polymer molecules. This strategy is mainly designed for highly ordered polymer with high stiffness at room temperature. After flow coating, the polymer backbone is mainly oriented along the coating direction.

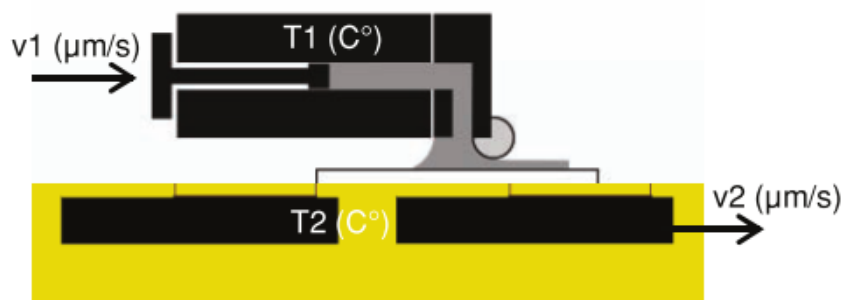


Figure.10 Schematic of flow-coating pBTTT^[36]

High temperature rubbing is another effective method to align crystalline polymer. The crystalline of pBTTT polymer experiences phase change at elevated temperature. pBTTT film is spun-coated and placed on hot plate at high temperature. When phase transition temperature is reached, rigid polymer side-chain begins to melt and plasticity of polymer film is greatly increased. Rotating cylinder is used to rub film surface and polymer backbone is aligned in the rubbing direction.

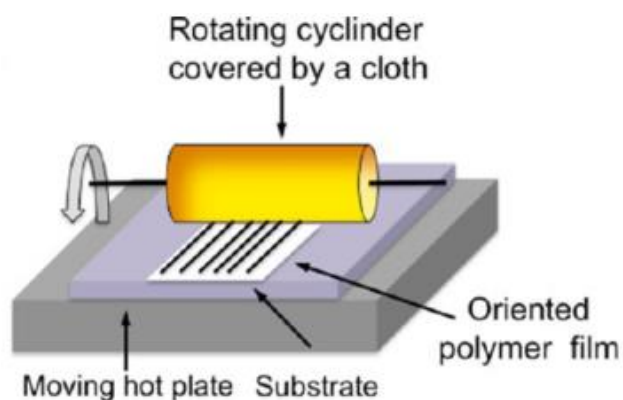


Figure.11 Schematic of rubbing pBTTT^[20]

2.2 pBTTT Morphology

As cast pBTTT polymer shows relatively isotropic morphology with small domains; upon thermal annealing, side-chains begin to melt at first transition temperature (around 145°C) (**Figure.12**) and film enters liquid-crystal phase, forming large terraced domains ^[35] (**Figure.13(b)**); Further annealing pBTTT film above its second transition temperature above 250°C often results in a unique nano-ribbon like highly ordered morphology (**Figure.13(c)**). In the ribbon-phase morphology, extended polymer backbones align next to each other in π stacking directions, forming extended ribbons with ribbon width being the length of backbone.^[21,36] Aligned pBTTT films that are annealed through its ribbon-phase threshold temperature show significant charge transport anisotropy, with aligned direction being the more favorable charge transport direction.^[36] This is attributed to the low resistance that charge encounters when hopping along backbone along align direction than in perpendicular direction and the different grain boundaries features in aligned films.

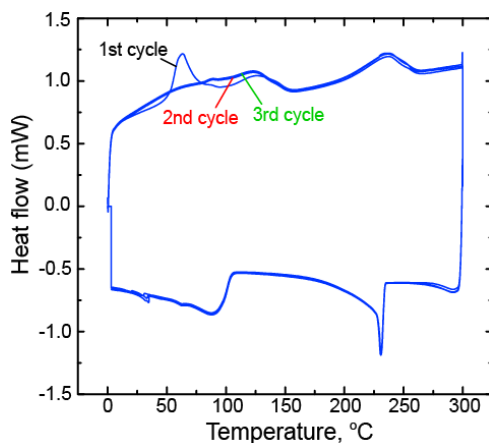


Figure.12 DSC of pBTTT used in this study

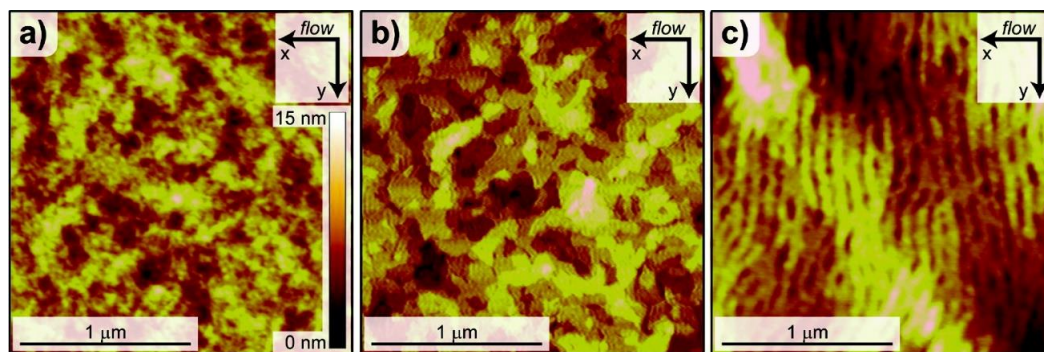


Figure.13 AFM images of pBTTT films after flow-coating (a) after casting, (b) terraced morphology, and (c) oriented ribbon shape.^[21]

In this study, we employ an improved strain align method. We demonstrate that when pBTTT films are under applied strain, in-plane aligned morphology can be achieved while showing large terraced domains. Different from flow coating aligned ribbon-phase pBTTT films that show significant grain boundaries between nano-ribbons, strain aligned terraced pBTTT shows large domains throughout film surface. With some dewetting observed, strain aligned pBTTT based OTFT shows high hole mobility up to $1.67 \text{ cm}^2\text{V}^{-1}\text{s}^{-1}$, which is one of the highest mobility reported for this system.^[9,10] The strain-aligned polymer, for the first time, provides an opportunity to study the charge transport feature in biaxial orientated conjugated polymer with improved local molecular order.

3. Experimental

3.1 Film Preparation

The pBTTT was synthesized using a previously reported method^[21] and had an average molecular mass is 26 kg/mol with polydispersion of 2.0 as measured by GPC in chlorobenzene a 80°C against polystyrene standards. The polymer was dissolved in a solvent pair of chloroform and 1,2-dichlorobenzene with a volume ratio of 1:1 at a concentration of 3 mg/ml. The solution was then spun cast hot (temperature of approximately 65 °C) onto OTS treated Si substrates at 1200(2 π) rad/min (1200 rpm) for 40 s. The solution casting process was conducted in a nitrogen filled glove-box.

3.2 Strain-Align and Transfer

Strain aligning conjugated polymer poly(3-hexylthiophene)(P3HT) has been reported in previous studies.^[22-25] P3HT can be strained at room temperature up to 140% due to its high ductility^[23]. pBTTT, however, due to its tight intermolecular bond between rigid alkyl side-chain, has a crack onset of below 2.5% at room temperature.^[23] Further strain will result in cracked films and a decrease hole mobility. But elevated temperature can melt alkyl sidechains and increase pB TTT film ductility and make strain-aligning possible.

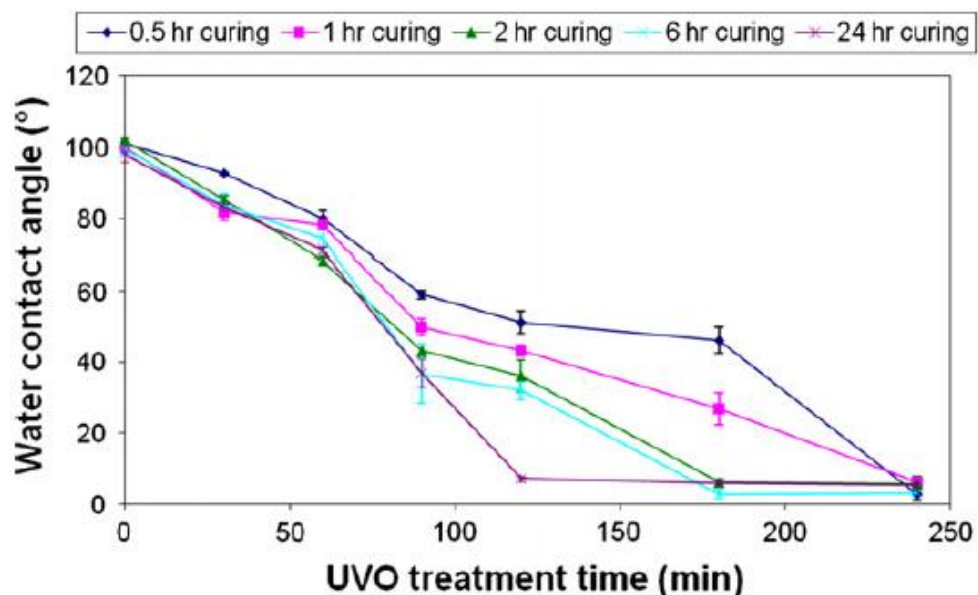


Figure.14 The effect of curing time on surface hydrophilization process of PDMS at 80°C ^[40]

Pristine PDMS is highly hydrophobic as can be characterized by contact angle. (Figure 14-15). Under elevated temperature, films will form dewetting severely. Due to the highly hydrophobic surface, PDMS slab is rendered to UV/Ozone treatment for 16 min prior strain to minimize film dewetting^[41,42].

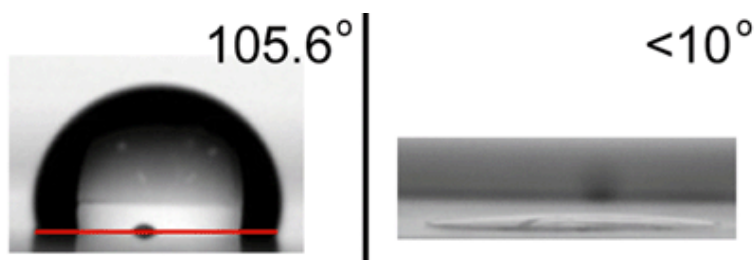


Figure.15 Contact angle of PDMS before and after UV Ozone treatment^[43]

UV/Ozone will promote silicon dioxide formation on PDMS slab surface and reduce contact angle, but also limit applied strain below 50% since further strain will usually result in crack on PDMS surface. We first transfer as cast pBTTT film onto host UV-Ozone treated PDMS slab whose both ends are clamped on a customized strain stage in our lab. Strain stage is then placed face down on a hot plate at an elevated temperature around 145°C (to let film reach a phase transition temperature of 120°C). After about 90s, film is applied desired strain up to 60%. Strained film is then transferred onto a cleaned native silicon substrate (this substrate is placed on hotplate during film is being heated to facilitate transfer). Strained film is then again transferred via a pristine PDMS onto octyltrichlorosilane (OTS) modified transistor substrate or glass. All transistor test-bed used in this study are treated in OTS environment for 12 to 16 hours to achieve hydrophobic surface to achieve optimum charge transport interface and highly edge-on molecular packing (conjugated ring plane perpendicular to substrate plane) as reported in previous study.^[37] The OTS solution consisted of 0.002mol/L OTS in anhydrous hexadecane. The strain and transfer process is demonstrated in **Figure.16**. Double transfer process requires film to be transferred from high-energy surface onto low-energy surface. After transfer process, strained film are left as-cast or annealed at 180°C for 2min.

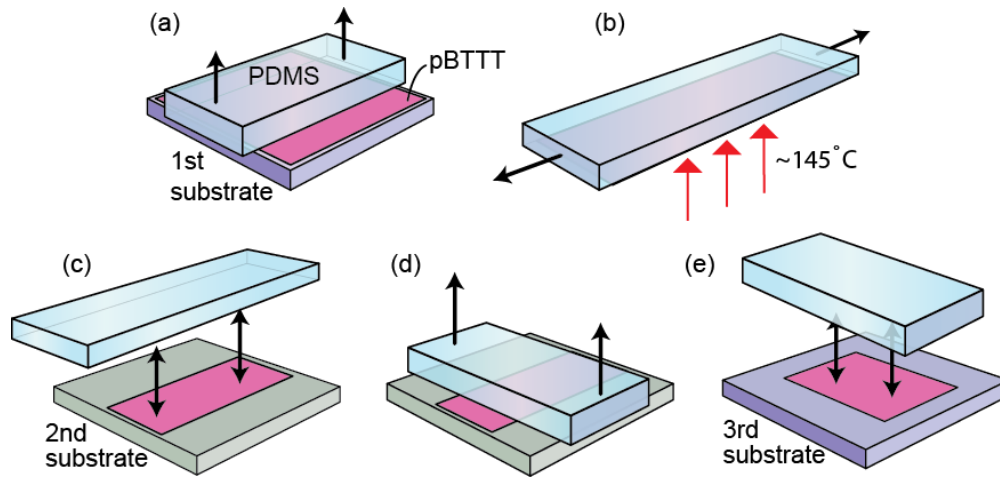


Figure.16 Strain and transfer schematic

3.3 Transistor Device Fabrication and Characterization

Here we characterize the charge transport in strain aligned pBTTT films using a bottom-gate bottom-contact transistor configuration. The transistor substrates were fabricated by thermally evaporating Ti/Pt (4 nm/35 nm) [or Ti/Au (4 nm/35 nm)] electrodes onto highly doped p-type Si wafer with 200 nm SiO₂ gate dielectric. Channel length of the OTFTs varied from 5 μm to 100 μm and the channel widths from 500 μm to 1000 μm. The room-temperature transistor characterization was done on high work function Platinum electrodes using HP 4156B semiconductor parameter analyzer in a Nitrogen filled environment. Transfer characteristics were measured with gate voltage swept from 20V to -60V under source-drain voltage being -70V. Saturated mobility was calculated by using linear fit of $I_{DS}^{1/2}$ versus V_G , from a range of 5 V. The uncertainty was estimated by taking one standard deviation of at least 3 devices and typically 4 to 6 devices.

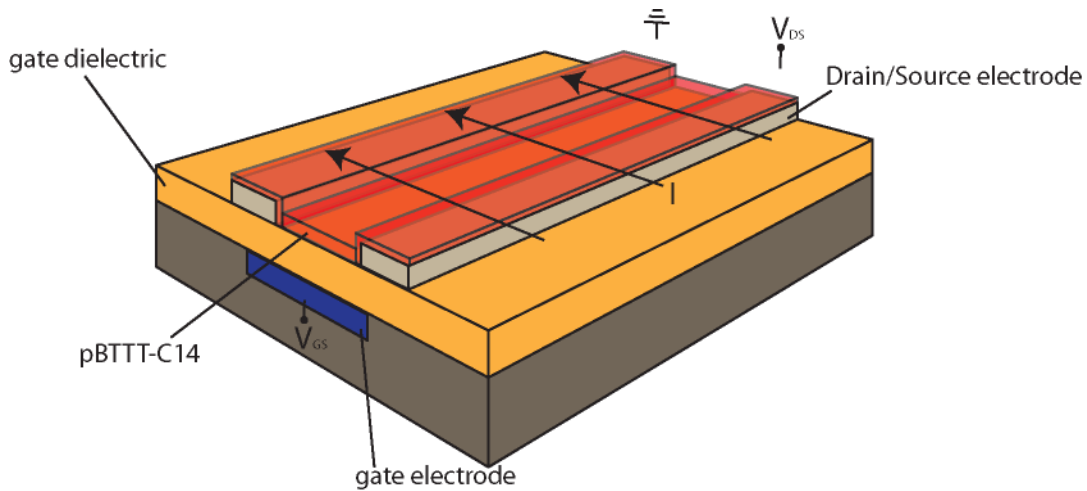


Figure.17 schematic of pBTTT bottom-gate bottom-contact transistor

Linear and saturated mobility are extracted as follows:

$$\text{Linear: } I_D = \mu \frac{W}{L} C_i (V_{GS} - V_T) V_{DS}$$

$$\text{Saturated : } I_{Dsat} = \frac{1}{2} \mu_{sat} \left(\frac{W}{L} \right) C_i (V_{GS} - V_T)^2$$

3.4 Morphology Characterization

For morphology characterization, as cast or strain pBTTT thin films are transferred onto oxide or OTS treated substrated (glass or native silicon). The UV-visible absorbance was measured using an Ocean Optics Jazz spectrometer. X-ray diffraction was performed at the Stanford Synchrotron Radiation Lightsource (SSRL) on beam line 11-3 with an area detector (MAR345 image plate), an energy of 12.735 keV, and an incidence angle of $\approx 0.12^\circ$. The atomic force microscope (AFM) images were measured with a Bruker Dimension 3000 in tapping mode. The DF-TEM imaging was conducted with a Philips EM400T transmission

electron microscope, operated at 120 kV. The images were recorded with an SIS Cantega 2 K CCD camera.

3.5 Low Temperature OFET Measurement

50% strained and as cast pBTTT bottom-gate bottom-contact device fabricated with Au electrodes are tested under room temperature. The channel length is 5 μm . The measured is annealed above its liquid-crystal transition temperature. The low temperature mobility was measured with an Agilent 4155C semiconductor parameter analyzer in a Lakeshore low-temperature probe station. The temperature was stepped at 20 K increments at a ramp rate of 1 K/min while keeping the samples under a vacuum of 10^{-6} torr and using liquid nitrogen as the cryogen. At each temperature step, the I_{DS} was measured while sweeping the gate voltage from 20 V to -60 V and setting the source-drain voltage at -60 V.

4. Result and Discussion

4.1 UV-Vis Absorbance

To characterize strain aligned pBTTT film, we first execute UV-Vis absorbance measurement of samples. The strained pBTTT films are printed onto unmodified pristine glass or OTS treated glass substrates. Absorbance of a 60% strained sample on pristine glass substrates is shown in **Figure.18(a)**. Incident light was polarized through a polarizer onto sample, then the light is collected by detector placed on the other side of sample. We find when incident light is polarized parallel to strain direction, absorbance is higher than when incident is perpendicular to strain direction. As previous study has revealed that optical transition dipole moment is along polymer backbone direction^[21], the anisotropic absorbance indicates that pBTTT polymer backbones are aligned in applied strain direction. In **Figure.18(b)**, Dichroic Ratio is plotted with different strain from 0% to 50%. Here the dichroic ratio (R) is defined as $R = A_{\parallel} / A_{\perp}$, where A_{\parallel} is the absorbance of light polarized parallel to the strain direction, and A_{\perp} is the absorbance of light polarized perpendicular to the strain direction (both taken at 550 nm). We can see R is highest for pristine (oxide) glass based sample for different strain levels. Annealed samples have higher Dichroic Ratio than as cast ones, corresponding to absorbance in **Figure.18(a)**. As cast strained film has a Dichroic ratio up to 2.2; in comparison, films that have been annealed to cycle through liquid-crystal phase change show a higher dichroic ratio up to 8.4 on unmodified glass, 4.8 on OTS modified glass substrate. The origin of this increase of dichroic ratio before and after thermal annealing is not fully understood so far. One possible explanation is alignment initially takes

place at the interface between film and PDMS host slab. The strained film is then transferred onto substrate and annealed, and the top aligned layer of the film serves as template and registry the bulk of the film. At a temperature above phase I transition temperature, alkyl side chains begin to melt and vertical registration happens from top to bottom, thus increase the alignment of the whole strained film. During the cooling process, melted alkyl chain will become rigid again. During this process, large terraced domain is formed and alignment is enhanced. This is similar with flow-coating aligned pBTTT; after annealed through the second transition temperature, pBTTT film will form highly ordered ribbon-phase with an increased dichroic ratio. It is speculated that the initial aligned crystal layer on top templates vertically the whole film in annealing process.^[36,39] Comparing films annealed on OTS treated glass substrate and pristine glass, we find a higher dichroic ratio on unmodified substrate. We speculate that during annealing films on OTS treated surface, low surface energy is less effective in restricting polymer and entropic driving forces result in limited macro order; meanwhile on unmodified surface higher surface energy strongly restrict polymer thus increase macro in-plane alignment significantly. 60% strained films show a similar dichroic ratio with flow-coated ribbon-phase pBTTT film.^[36]

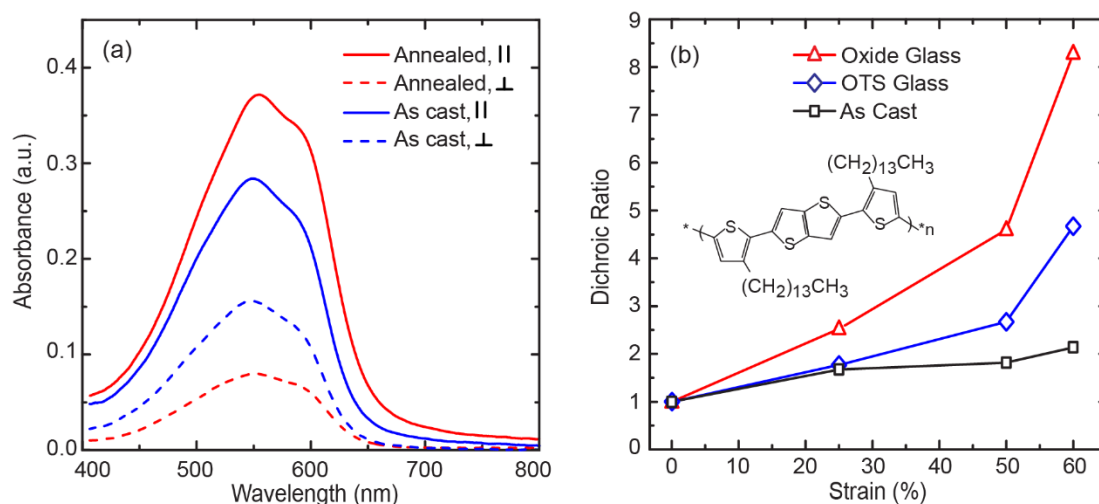


Figure.18 Absorbance and dichroic ratio vs strain

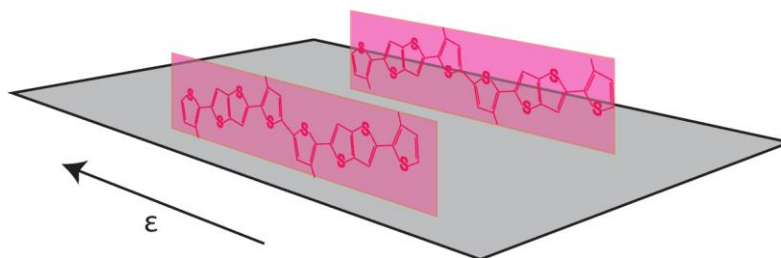


Figure.19 Schematic of pBTTT backbone alignment

4.2 GIXD

To gain a further insight into strain aligned pBTTT morphology, we use grazing incidence X-ray diffraction (GIXD) with 2D-images to characterize crystalline stacking, as shown in **Figure.20**. For the spun cast films, the diffraction characteristics are similar to previous reports showing strong out of plane (h00) peaks.^[15,35] These peaks become more

focused after thermal annealing indicative of highly edge-on stacking.^[15] Significant diffraction is also observed near in-plane scattering vector (q_{xy}) of 1.41 Å, and 1.71 Å, that move vertically on the image plates. This diffraction has previously been attributed to (21-1), (h13), and (h10) indices with additional details given in Cho et al.^[44] GIXD images are also shown for a 25 % and 50 % strained film with the incident X-ray beam parallel (scattering vector nominally perpendicular) and X-ray beam perpendicular (scattering vector nominally parallel) to the strain direction. The strained films continue to have sharp (h00) out-of-plane peaks indicative of edge-on stacking. As the film is strained, the off-normal scattering is shown to depend on sample orientation with (h10) peaks being significantly larger for the scattering vector perpendicular to the strain direction, and (h-13) peaks being larger for the scattering vector parallel to the strain direction. This anisotropic scattering behavior is similar to biaxial oriented ribbon-phase pBTTT films achieved through flow coating.^[44] Qualitatively, the diffraction anisotropy appears to be greater in the flow-coated films, consistent with the larger dichroic ratios.

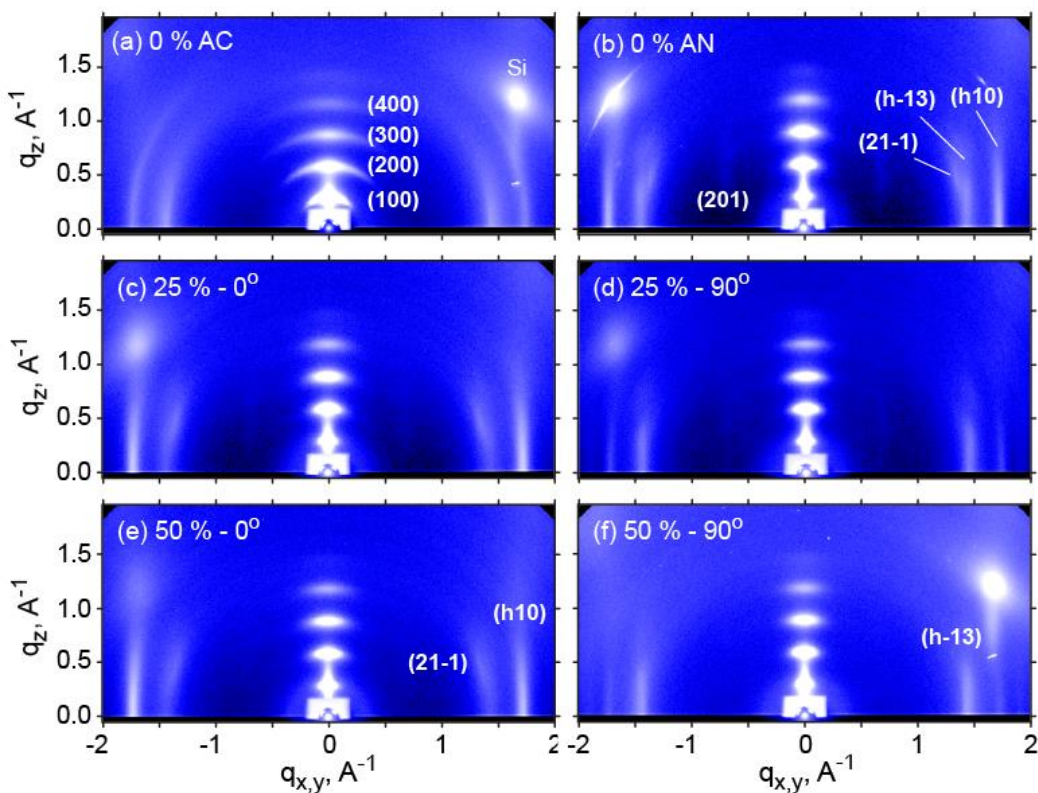


Figure.20 GIXD, 2-D image plate data for pBTTT films.

4.3 AFM

As cast pBTTT films typical form large crystalline terraced domains while being annealed through its first meso-phase transition temperature on OTS treated hydrophobic substrate. Further elevate anneal temperature will results in ribbon-like morphology which initiates from top of film in both isotropic and biaxially orientated films.^[36] It is interesting to examine annealed strain aligned pBTTT film in tapping mode atomic force microscopy (AFM). The atomic force microscope images were measured with a Bruker Dimension 3000 in tapping mode. AFM images of 0%, 25% and 50% strained films annealed at 180°C for 2

mins on OTS treated surface are shown in **Figure.21(a)-(c)**. We see annealed as cast film show large terraced domain that forms from liquid crystal phase; meantime, annealed strained aligned films show terraced morphology with similar domain size, in 200nm scale. This is quite interesting when compared with previous research showing that flow-coating aligned pBTTT show similar terraced morphology at this annealed temperature.^[21] In **Figure. 21(d)(e)**, 50% strained films are measured in a 5 μm x 5 μm scale showing terraced feature. It is worth pointing out that the void in the images are due to dewetting during thermal annealing. Dewetting is observed constantly throughout characterization. Since films are strained at elevated temperature, and film thickness becomes thinner after stretch, there are some potential cracking spots throughout film surface. Although film dewetting is minimized by rendering PDMS host slab in UV-Ozone environment, slight dewetting will also happens in strain process. More dewetting happens later during liquid-crystal annealing on OTS treated surface. The dewetting will most likely initiates from the “potential cracking” that already exists from stretching and grows bigger with longer annealing time. This explains why there are more dewetting observed on strained films than on as-cast films. Although UV-Ozone treatment increases PDMS hydrophilicity and reduces film dewetting effectively, it also limits the elasticity of PDMS since higher strain than 55% results PDMS surface cracking and further results in cracked films. Larger amount of dewetting is observed on higher strained films. Previous studies also reported dewetting for this system^[35,36] on hydrophobic surface.

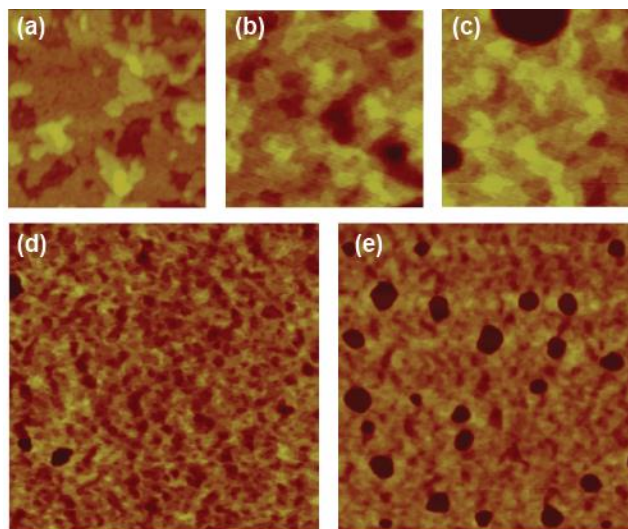


Figure.21 Tapping-mode AFM images of (a) spin-cast, (b,d) 25 % strained, (c,e) and 50 % strained pBTTT-C14 films on OTS silicon.

4.4 TEM

AFM images of annealed films show large terraced morphology on film surface, but not sufficient morphology details about molecular packing or polymer alignment through entire polymer thickness. Here we use dark-field transmission electron microscopy (DF-TEM) to create film diffraction pattern and then use 8 pixel method to show molecular orientation in orientation map as previously reported.^[45] DF-TEM images capture the electron diffraction character of the crystalline polymer where image contrast is based on the orientation of in-plane diffraction. Generally in polymer films with no large-scale preferential in-plane orientation, TEM diffraction from the variously oriented crystals result in a ring pattern, shown in **Figure.22(a)** for a spun cast film. As the film is strained, the diffraction forms arcs associated with the level of in-plane alignment, as shown in **Figure.22(b, c)** for the strain-

aligned films. By tilting the beam such that only a specific arc of the diffraction can pass through a centered objective aperture, contrast based on local crystal orientation can be captured. The image created on the image plane of the objective lens with the tilted beam is thus brightest for the quasi-domains that were oriented so that their diffraction spots could pass through the aperture. By tilting the beam in a number of different orientations, the various crystal contributions that make up the diffraction ring is mapped. Here we use the diffraction corresponding to (h10) peaks [primarily (0-10) and (110)]^[44] corresponding to π - π stacking to map the crystal orientation as this corresponds to the most intense peaks. The beam tilt was adjusted away from the sample surface normal such that the 30 μm aperture would admit a range of the (h10) ring encompassing an arc of approximately 90°. By acquiring multiple images from the same specimen area but with different beam-tilt configurations, and associating the intensity pattern each pixel displays with its in-plane crystal orientation, a color-coded orientation map can be created with results shown in **Figure.22** for a spun cast as well as 25 % and 50 % strained films.

The TEM orientation map of the spun cast (unstrained) film is similar to a previous demonstration by Zhang et al.^[45] with quasi-domains of approximately 700 nm (obtained by Fourier transform analysis). These domains are similar to the terraces measured with AFM. The well-defined areal pattern shows that there is a common orientation of polymer chains vertically through the film.^[45] In the unstrained film, the colors ascribed to the domains are not distributed equally, i.e., there appear to be major and minor colors, which has been attributed to the fact that they correspond to two sets of intensity patterns that represent different amounts

of pixels.^[45] Thus, no significant long-range in-plane alignment of the polymer backbone is found in the spun cast films. For the strained films, the selected aperture areas for color mapping are only chosen where there is significant (h10) diffraction and other areas are not assigned a color (left as black). For the 25% strained film, the quasi-domains remain similar to the unstrained films, but now preferential alignment of the domains is observed. In the 50 % strained films, the quasi-domains are present but appear to decrease in size, particularly near locations of film dewetting. The TEM images also show an increasing number of holes in the films with applied strain similar to that observed by AFM. The holes appear as black spots in the DF-TEM images, and are also observed in the corresponding bright field TEM images shown in **Figure.22**. In comparison, holes are rarely observed in as cast films. Thus, the selected aperture positions effectively map the orientation of the diffracting polymer in the film. We find that in the strained films the in-plane texture continues to have a nematic stacking character, as previous indentified for spun cast pBTTT films.^[45] Also of note is that a closer look at the polymer orientation near the holes in the film shows that the polymer backbone is oriented tangentially at the edge of the holes, within the resolution of the orientation mapping.

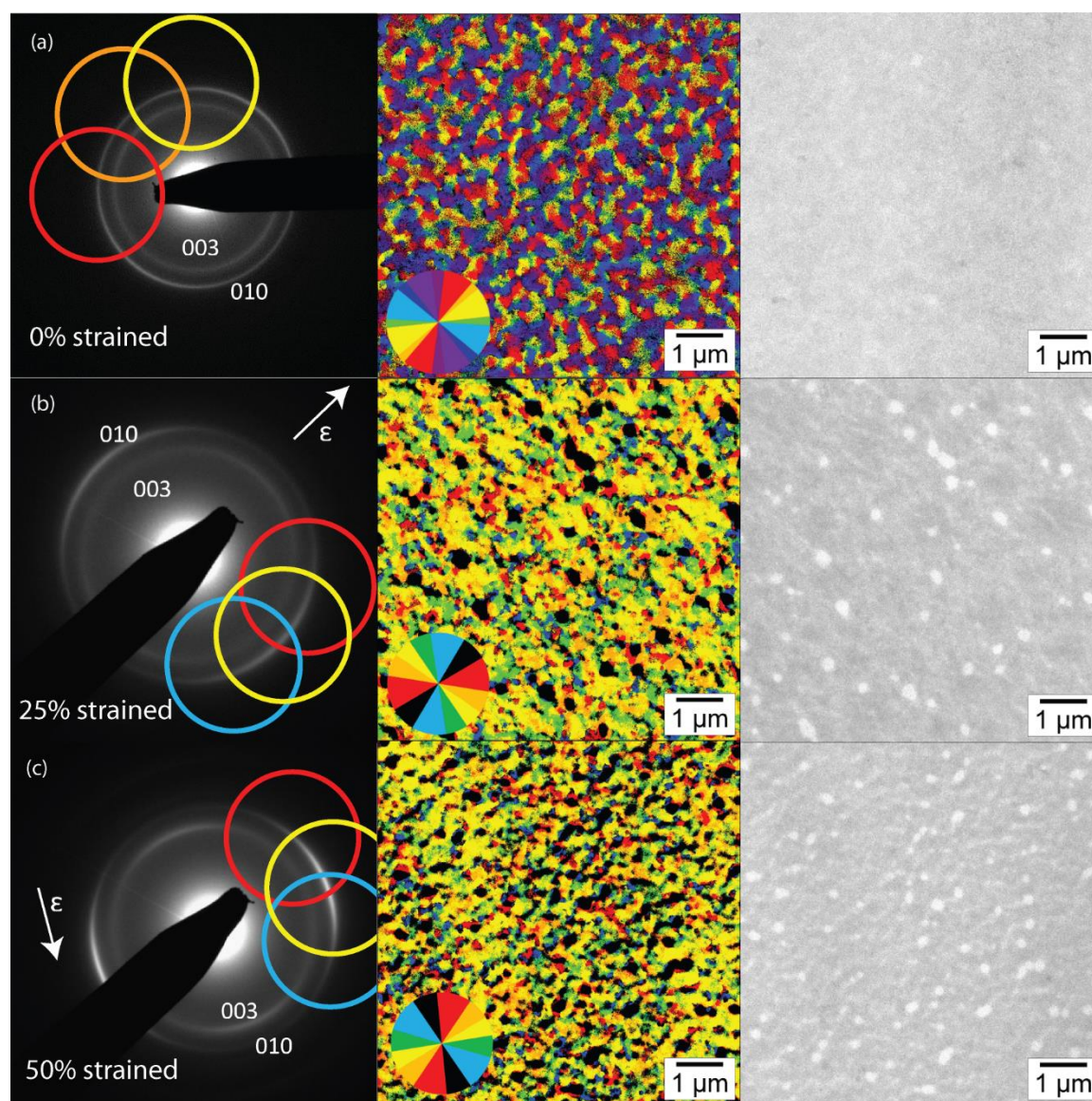


Figure.22 Diffraction patterns and dark field images for (a) unstrained pBTTT film, (b) 25% strained film, (c) and 50 % strained film.

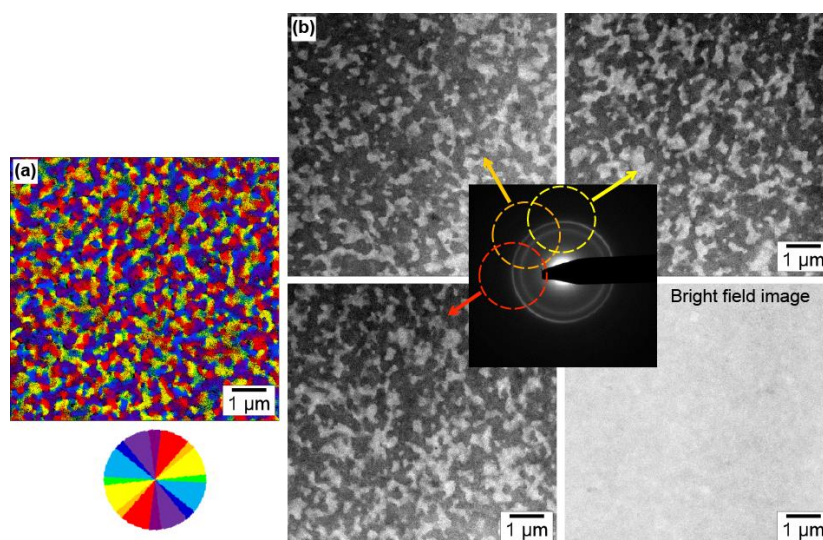


Figure.23 TEM color orientation map and diffraction pattern of 0% strained pBTTT film

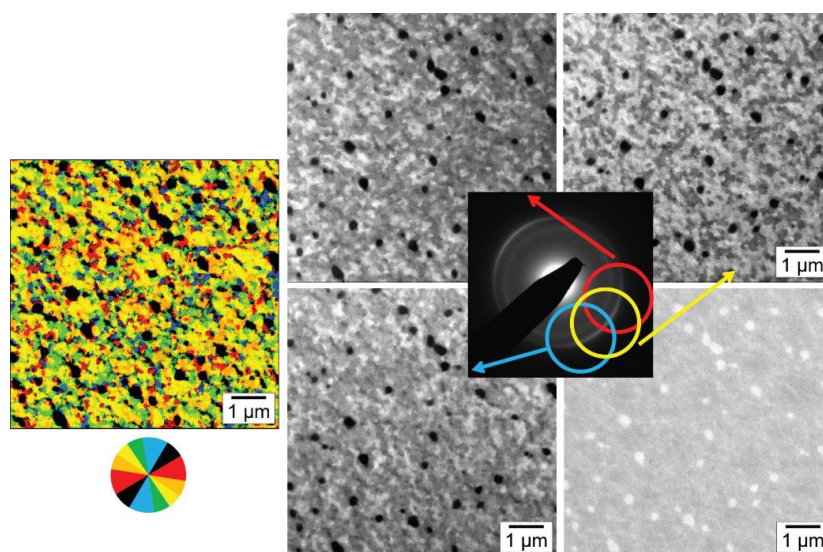


Figure.24 TEM color orientation map and diffraction pattern of 25% strained pBTTT film

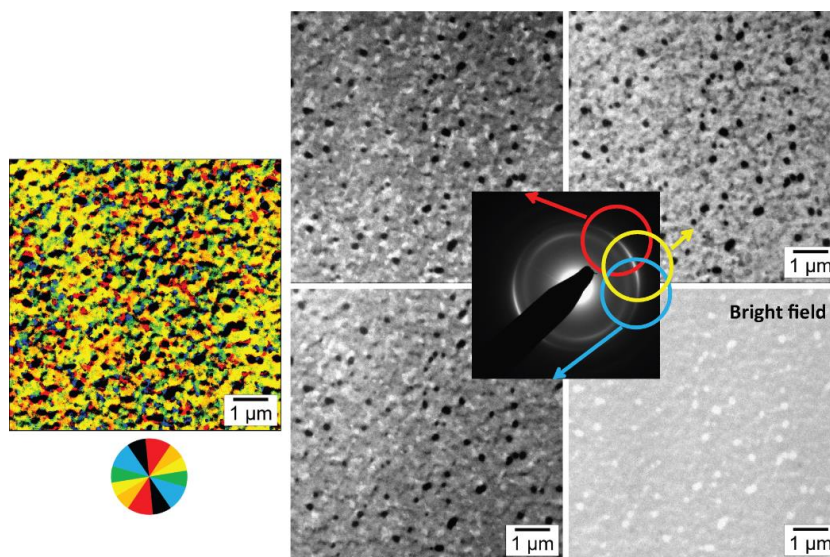


Figure.25 TEM color orientation map and diffraction pattern of 50% strained pBTTT film

From the above morphological characterizations, we can see strain aligned pBTTT film shows highly anisotropic morphology, with polymer backbones aligned in strain direction. After strained films are annealed on hydrophobic substrate surface, it maintained highly ordered large crystalline terraced domain similar to isotropic film; and this terraced morphology is known for its efficient charge transport.^[35] By comparing films before and after annealing, we find thermal annealing increases film macro order and polymer backbone alignment. Further GIXD and TEM diffraction patterns provide direct chain alignment proof of molecular orientation for strained films with highly edge-on morphology. Although strain aligned pBTTT shows a lower dichroic ratio of 4.8 on OTS substrate than aligned ribbon-phase pBTTT(up to 10), it maintains larger terraced low-angle quasi-domains; DF-TEM and AFM suggest terraced quasi-domains show less significant grain boundaries, In contrast,

highly aligned ribbon-phase films consist of more disordered, consistent grain boundaries between fully-extended polymer backbones; ribbons are supposed to connect with each other with a limited number of molecular tie-chain coupling.

4.5 Room Temperature Charge Transport Characterization

Comparing isotropic device with strain-aligned devices (channel length =5 μ m), we see that saturated mobility along strain direction (parallel) increase with higher applied strain from 0% to 50%; meanwhile saturated mobility is higher in along strain direction than perpendicular direction (**Figure.28**). Here isotropic devices exhibit similar mobility with earlier study.^[9] This is consistent with our speculation that polymer backbone is aligned along strain direction since along backbone is more efficient charge transport path. Previous study reported strain aligned conjugated P3HT polymer with similar feature.^[24] Mobility anisotropy up to 6.5 has been observed in 50% strained device. By looking at transfer characteristics of 50% strained (parallel) and isotropic devices (**Figure.28**), we can see high on/off ratio of 10^8 and threshold voltage near 0 V; isotropic devices show an on/off ratio of 10^7 and threshold voltage near 15 V. Film thickness may also be another factor account for this difference since it affects short channel devices more than long channel devices. The difference in on/off ratio and threshold voltage becomes smaller in long channel isotropic and strained devices. Also strained devices tend to have more dewetting along the “thin part” created during strain. These dewetting makes strained films and isotropic films have quite different morphology which accounts for part of the difference in charge transport. Despite more dewetting observed in strain aligned devices, strain-aligned short channel devices show

a higher saturated mobility than isotropic devices. We have extracted mobility up to $1.67 \text{ cm}^2\text{V}^{-1}\text{s}^{-1}$ (the average was $1.52 \text{ cm}^2\text{V}^{-1}\text{s}^{-1}$) from 50% strained $5 \mu\text{m}$ channel length devices(parallel), representing one of the highest mobility reported for pBTTT based OFET.^[9,10]

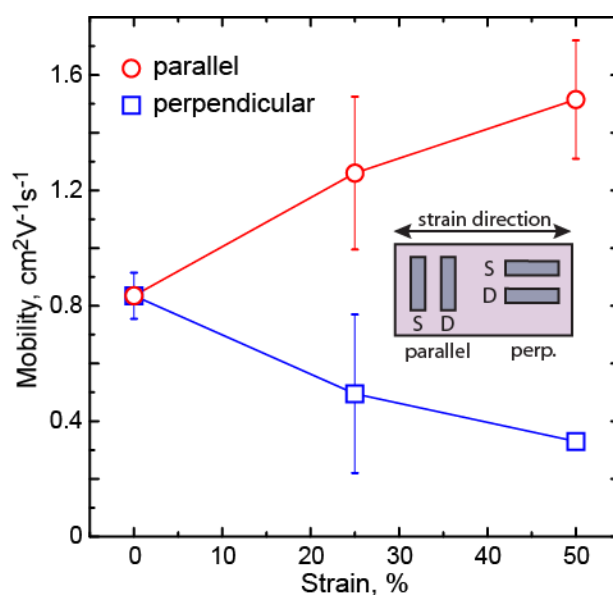


Figure.26 Mobility vs strain. (a) Saturated field-effect mobility of pBTTT films strained by 0 %, 25 % and 50 %. Transistor channel length is $5 \mu\text{m}$.

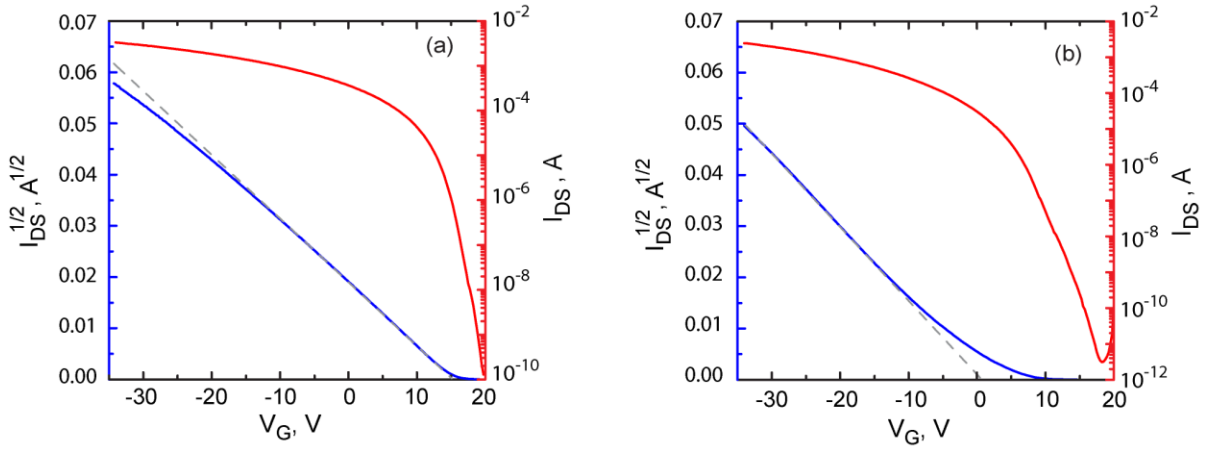


Figure.28 Source-drain current (I_{DS}) for OTFTs for a spun cast films (a) and a 50 % strained film (b).

The channel length dependence of saturated mobility in both parallel and perpendicular to strain direction are shown in **Figure.29-31**. Saturated mobility is given in $\mu = \mu_0 \exp[\gamma^* E^{1/2}]$, where μ_0 is the zero-field mobility, γ is scaling prefactor, and E is the applied electric field. The fitting parameters are shown in **Figure.29**. Here we take $E = V_{DS}/L$, $V_{DS} = -70V$. This estimation method is verified elsewhere, based on that about 80% field in OFET channel is constant.^[46] We can see saturated mobility fits well into Poole-Frenkel model. Previous study already found that mobility of isotropic liquid-crystal pBTTT based OFET (Au or Pt) fits well in Poole-Frenkel model.^[9,46] Here we find γ increases with applied strain in parallel to strain direction. In perpendicular to strain direction, γ maintains relatively constant. Looking back similar studies, we find the value of γ is closely related to polymer film order. Hamadani found that γ increases after pBTTT is annealed above its liquid-crystal transition temperature^[46]; Gargi used a similar strain method to align P3HT and

found in strained film γ is higher than unstrained film.^[25] The increase of γ suggests a stronger mobility field dependence in saturated regime. The origin of γ is supposed to be caused by the combination of polymer backbone order and local disorder within grain boundaries. However, for parallel direction we observe a stronger field dependence which may indicate the backbone alignment is a dominant contribution to this phenomenon in strain aligned devices. In relatively amorphous as cast devices, there is no favored orientation direction, saturated mobility is a combination of transport along backbone and π - π coupling directions. Recent research reveals that paracrystallinity disorder induces traps in charge transport^[47,48] and may account for the observed change of value in as cast and strained devices.

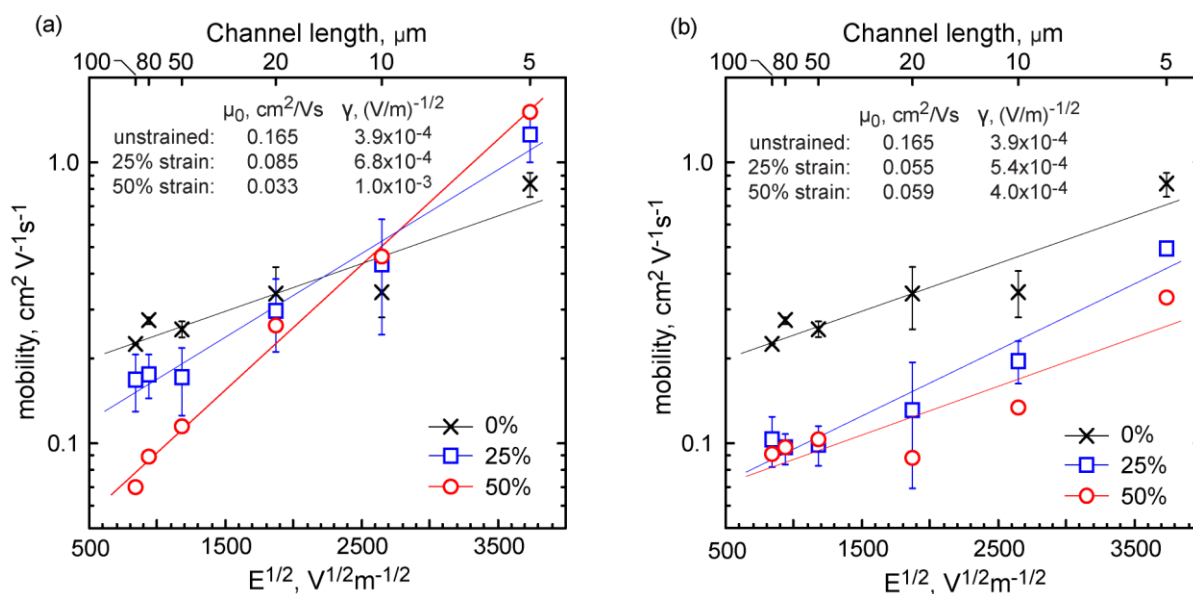


Figure.29 The saturated mobility with applied field (a) parallel to the strain direction strained film. (b) perpendicular to the strain direction

The origin of Poole-Frenkel (PF) effect is not well understood so far, it has generally been attributed to the disorder that cause the field drop in device channel. Recent studies reveal that the commonly observed PF behavior is related to the disorder exist in organic polymer semiconductor. Novikov et al proposed that electric dipole moments in amorphous organic semiconductor cause fluctuation in charge carrier potential energy and this fluctuation accounts for field dependence^[49]; Yu and co-workers show that thermal fluctuation modifies energy levels and the steric restoring forces correlates with localized electronic states energies.^[50]

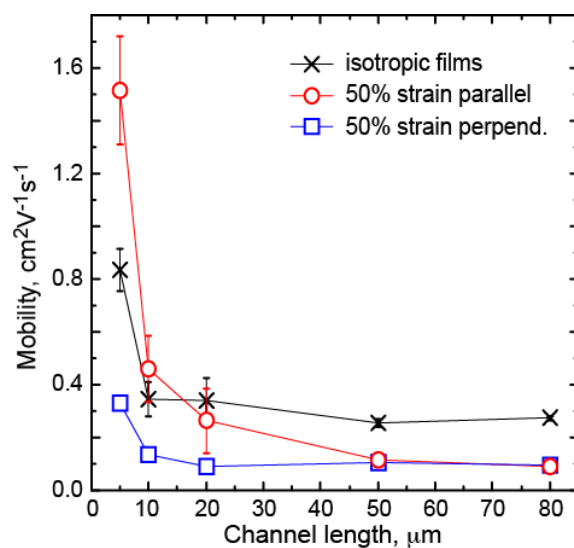


Figure.30 Channel length dependence (0% and 50% strained)

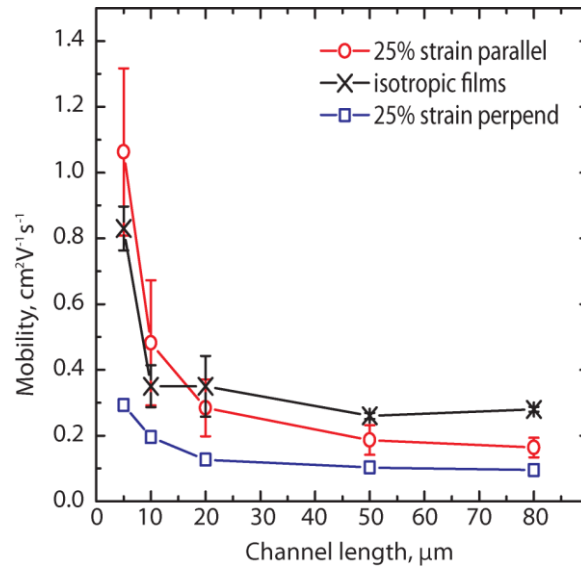


Figure.31 Channel length dependence (0% and 25% strained)

4.6 Low Temperature Charge Transport

In **Figure.32**, saturated mobility is plotted as function of temperature. The activation energy was estimated using Arrhenius equation. Saturated mobility for strained device and as cast device generally keeps the same trend throughout the temperature sweep, with parallel direction shows highest mobility, perpendicular direction the lowest. Activation energy(E_A) is extracted from 180K to 120K. We find activation energy is lowest in parallel to strain direction(21.2 meV) while highest in perpendicular direction(34.3 meV). It is consist with the higher mobility in parallel direction and represents a more efficient charge transport mechanism. It is interesting to point out that in parallel direction E_A is similar to that in as cast device, but in perpendicular direction E_A is found to be about 50% higher. The high activation energy suggests a major limit in charge transport mechanism introduced by strain process. The

trend that aligned device and as cast devices show here is similar to that found in ribbon-phase pBTTT under room temperature.^[36] From the range of 300K -200K, the mobility deviates from the Arrhenius equation, showing a downward curve. similar behavior has been reported on pBTTT,^[36,51] which is attributed to residual moisture. Some other organic semiconductor also show similar deviation^[52-54] and they are attributed to structural relaxation in the polymer^[52], bias-stress effect^[55] and residual moisture. ^[56]

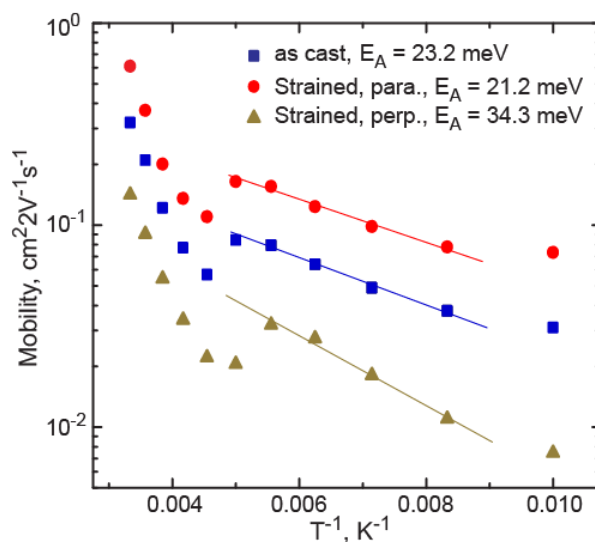


Figure.32 Saturated mobility vs temperature. (0% and 50% strained)

4.7 Comparing Charge Transport in Oriented OTFTs with Au and Pt Electrodes

Strained pBTTT films are also printed onto transistor substrate with Au electrodes to fabricate bottom-gate, bottom-contact transistors. The extracted saturated charge mobility of

50% strained devices is plotted in **Figure.33**, in parallel (a) and perpendicular (b) directions. We can see for short channel devices ($5\mu\text{m}$ - $20\mu\text{m}$), parallel strained Pt devices show higher mobility than Au devices. For longer channel devices, Au devices show a higher mobility. A similar data is also observed in previous study for pBTTT,^[9,57] and this is attributed to the difference in work function between Pt and Au. The high function of Pt results in short channel devices are less affected by contact resistance but dominated by channel resistance. For low work function Au devices, contact resistance is a dominant factor for all channel length. As we can see Pt devices show a much stronger mobility channel length dependence.

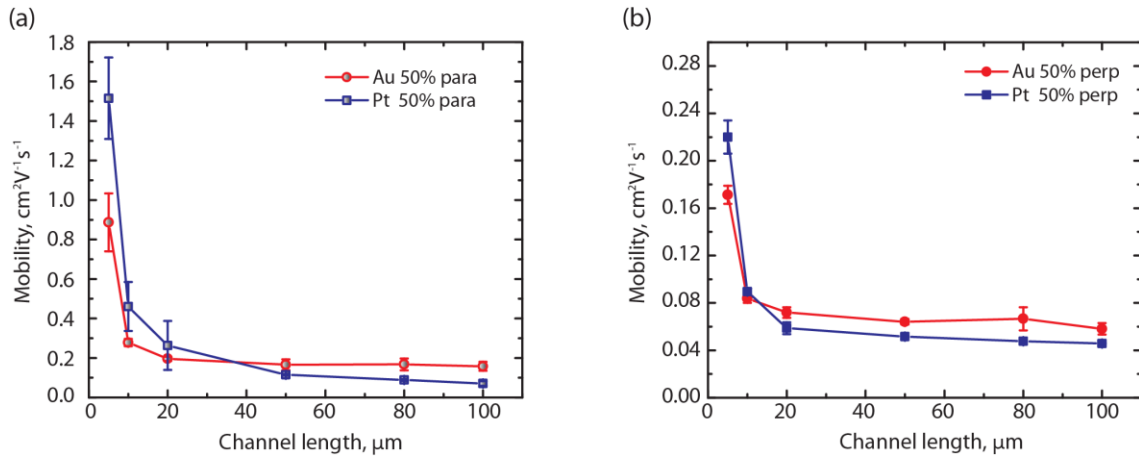


Figure.33 Channel length dependence of the saturated mobility for 50% strained films (Au VS Pt)

Some research has been conducted on both Au and Pt devices, but it is hard to quantitatively explain this difference in channel length dependence now. Maybe the contact resistance for

short channel device further complicates the charge transport in channel. The morphology of the strained films at contact and should be considered when extracting contact resistance.

5. Conclusion

In this study we demonstrate that using a modified strain method to strain organic polymer semiconductor pBTTT-C14 and result in biaxial orientated films. This strain method strains pBTTT at an elevated temperature that let film reach a temperature around its liquid-crystal phase transition temperature. The strained film is shown to have highly anisotropic morphology with polymer backbones aligned along the strain direction. Strain aligned films show a wide terraced morphology similar to as cast liquid crystal films. Compared with flow-coating aligned pBTTT with nano-ribbon like morphology, strained films show less significant grain-boundaries between quasi-domains. The size of quasi-domains increases with the amount of applied strain. Strained films exhibit a high dichroic ratio up to 8. Parasitic dewetting is observed on strained film. Despite the dewetting, we achieved a saturated mobility comparable to aligned ribbon-phase device. On 50% strained Au electrodes devices with channel length $L=20\mu\text{m}$, a saturated of $0.2\text{ cm}^2\text{V}^{-1}\text{s}^{-1}$ is extracted, which is similar to ribbon-phase counterpart.^[36] On Pt device, a record high mobility $1.67\text{ cm}^2\text{V}^{-1}\text{s}^{-1}$ is extracted on 50% strained device. Mobility in parallel to strain is increased by alignment and is usually 4 times higher than in perpendicular. This is achieved while limited by the amount of applicable strain and dewetting on films. The mobility values suggest the polymer backbones is effectively aligned and terraced morphology may be more favorable for charge transport. This is consistent with the fact that it shows larger domain size and less significant grain-boundaries. In ribbon-phase pBTTT, the gap between adjacent nano-ribbon is bridged by limited polymer backbones, this can cause deep charge trap within disordered

grain boundaries. DF-TEM measurement indicates that polymer backbones are aligned around dewetted part, providing an encircled path for charge transport. In this way it is speculated that dewetting has a limited impact on device performance. These well defined holes increase the contact area between active layer and environment and can be potentially applied in stretchable electronics and chemical sensors.^[58,59] Saturated mobility is found to fit Poole-Frenkel model well and the dependence gets stronger with larger applied strain in parallel to strain direction. It is speculated that the strong field dependence is due to polymer backbone alignment. The difference between aligned wide-terraced and ribbon-phase pBTTT provides a good chance to study the relationship between morphology and charge transport in conjugated polymer.

References

- [1] H. Shirakawa, J. Louis, A. G. Macdiarmid, *J. C. S. Chem. Comm* **1977**, 578.
- [2] http://education.mrsec.wisc.edu/SlideShow/slides/pn_junction/konarka.html.
- [3] solar cell.
- [4] <http://www.digitaltrends.com/home-theater/lg-officially-prices-4k-oled-tvs-2014/>.
- [5] D. J. Gundlach, *Nat. Mater.* **2007**, *6*, 173.
- [6] <https://upload.wikimedia.org/wikipedia/commons/9/90/ComplementaryTechnologies.png>.
- [7] A. Chortos, J. Lim, J. W. F. To, M. Vosgueritchian, T. J. Dussault, T. H. Kim, S. Hwang, Z. Bao, *Adv. Mater.* **2014**, *26*, 4253.
- [8] M. Shin, J. H. Song, G. H. Lim, B. Lim, J. J. Park, U. Jeong, *Adv. Mater.* **2014**, *26*, 3706.
- [9] B. H. Hamadani, D. J. Gundlach, I. McCulloch, M. Heeney, *Appl. Phys. Lett.* **2007**, *91*, 1.
- [10] S. Wang, A. Kiersnowski, W. Pisula, K. Mullen, K. Müllen, **2012**.
- [11] H. Sirringhaus, *Adv. Mater.* **2014**, *26*, 1319.
- [12] H. Dong, C. Wang, W. Hu, *Chem. Commun.* **2010**, *46*, 5211.
- [13] K. Myny, E. Van Veenendaal, G. H. Gelinck, J. Genoe, W. Dehaene, P. Heremans, *IEEE J. Solid-State Circuits* **2012**, *47*, 284.
- [14] H. Klauk, *Chem. Soc. Rev.* **2010**, *39*, 2643.
- [15] D. M. DeLongchamp, R. J. Kline, D. a. Fischer, L. J. Richter, M. F. Toney, *Adv. Mater.* **2011**, *23*, 319.
- [16] A. Salleo, R. J. Kline, D. M. DeLongchamp, M. L. Chabinyc, *Adv. Mater.* **2010**, *22*, 3812.

- [17] C. Huang, Y. Lan, *Chem. Eng.* **2010**, 2010.
- [18] J. Rivnay, S. C. B. Mannsfeld, C. E. Miller, A. Salleo, M. F. Toney, *Chem. Rev.* **2012**, *112*, 5488.
- [19] C. Y. Yang, C. Soci, D. Moses, a. J. Heeger, *Synth. Met.* **2005**, *155*, 639.
- [20] L. Biniek, N. Leclerc, T. Heiser, R. Bechara, M. Brinkmann, *Macromolecules* **2013**, *46*, 4014.
- [21] D. M. DeLongchamp, R. J. Kline, Y. Jung, D. S. Germack, E. K. Lin, A. J. Moad, L. J. Richter, M. F. Toney, M. Heeney, I. McCulloch, *ACS Nano* **2009**, *3*, 780.
- [22] B. T. O'Connor, O. G. Reid, X. Zhang, R. J. Kline, L. J. Richter, D. J. Gundlach, D. M. DeLongchamp, M. F. Toney, N. Kopidakis, G. Rumbles, *Adv. Funct. Mater.* **2014**, *24*, 3422.
- [23] B. O'Connor, E. P. Chan, C. Chan, B. R. Conrad, L. J. Richter, R. J. Kline, M. Heeney, I. McCulloch, C. L. Soles, D. M. DeLongchamp, *ACS Nano* **2010**, *4*, 7538.
- [24] B. O'Connor, R. J. Kline, B. R. Conrad, L. J. Richter, D. Gundlach, M. F. Toney, D. M. DeLongchamp, *Adv. Funct. Mater.* **2011**, *21*, 3697.
- [25] D. Gargi, R. J. Kline, D. M. DeLongchamp, D. A. Fischer, M. F. Toney, B. T. O. Connor, **2013**.
- [26] C. Luo, A. K. K. Kyaw, L. a. Perez, S. Patel, M. Wang, B. Grimm, G. C. Bazan, E. J. Kramer, A. J. Heeger, *Nano Lett.* **2014**, *14*, 2764.
- [27] H. R. Tseng, L. Ying, B. B. Y. Hsu, L. a. Perez, C. J. Takacs, G. C. Bazan, A. J. Heeger, *Nano Lett.* **2012**, *12*, 6353.
- [28] H. Sirringhaus, R. J. Wilson, R. H. Friend, M. Inbasekaran, W. Wu, E. P. Woo, M. Grell, D. D. C. Bradley, *Appl Phys Lett* **2000**, *77*, 406.
- [29] T. G. Bäccklund, H. G. O. Sandberg, R. Österbacka, H. Stubb, M. Torkkeli, R. Serimaa, *Adv. Funct. Mater.* **2005**, *15*, 1095.
- [30] Z. Hu, B. Muls, L. Gence, D. a. Serban, J. Hofkens, S. Melinte, B. Nysten, S. Demoustier-Champagne, A. M. Jonas, *Nano Lett.* **2007**, *7*, 3639.

- [31] H. R. Tseng, H. Phan, C. Luo, M. Wang, L. a. Perez, S. N. Patel, L. Ying, E. J. Kramer, T. Q. Nguyen, G. C. Bazan, A. J. Heeger, *Adv. Mater.* **2014**, *26*, 2993.
- [32] M. L. Chabiny, M. F. Toney, R. J. Kline, I. McCulloch, M. Heeney, **2007**, 3226.
- [33] D. M. DeLongchamp, R. J. Kline, Y. Jung, E. K. Lin, D. a. Fischer, D. J. Gundlach, S. K. Cotts, A. J. Moad, L. J. Richter, M. F. Toney, M. Heeney, I. McCulloch, *Macromolecules* **2008**, *41*, 5709.
- [34] D. M. DeLongchamp, R. J. Kline, E. K. Lin, D. a. Fischer, L. J. Richter, L. a. Lucas, M. Heeney, I. McCulloch, J. E. Northrup, *Adv. Mater.* **2007**, *19*, 833.
- [35] I. McCulloch, M. Heeney, C. Bailey, K. Genevicius, I. Macdonald, M. Shkunov, D. Sparrowe, S. Tierney, R. Wagner, W. Zhang, M. L. Chabiny, R. J. Kline, M. D. McGehee, M. F. Toney, *Nat. Mater.* **2006**, *5*, 328.
- [36] M. J. Lee, D. Gupta, N. Zhao, M. Heeney, I. McCulloch, H. Sirringhaus, *Adv. Funct. Mater.* **2011**, *21*, 932.
- [37] R. J. Kline, D. M. DeLongchamp, D. a. Fischer, E. K. Lin, M. Heeney, I. McCulloch, M. F. Toney, *Appl. Phys. Lett.* **2007**, *90*, 2055.
- [38] C. Wang, L. H. Jimison, L. Goris, I. McCulloch, M. Heeney, A. Ziegler, A. Salleo, *Adv. Mater.* **2010**, *22*, 697.
- [39] T. Schuettfort, B. Watts, L. Thomsen, M. Lee, H. Sirringhaus, C. R. McNeill, *ACS Nano* **2012**, *6*, 1849.
- [40] K. Ma, J. Rivera, G. J. Hirasaki, S. L. Biswal, *J. Colloid Interface Sci.* **2011**, *363*, 371.
- [41] Y. Berdichevsky, J. Khandurina, A. Guttman, Y. H. Lo, *Sensors Actuators, B Chem.* **2004**, *97*, 402.
- [42] A. Oláh, H. Hillborg, G. J. Vancso, *Appl. Surf. Sci.* **2005**, *239*, 410.
- [43] J. Wu, N. Y. Lee, *Lab Chip* **2014**, *14*, 1564.
- [44] E. Cho, C. Risko, D. Kim, R. Gysel, N. C. Miller, D. W. Breiby, M. D. McGehee, M. F. Toney, R. J. Kline, J.-L. Bredas, *J. Am. Chem. Soc.* **2012**, *134*, 6177.
- [45] X. Zhang, S. D. Hudson, D. M. DeLongchamp, D. J. Gundlach, M. Heeney, I. McCulloch, *Adv. Funct. Mater.* **2010**, *20*, 4098.

- [46] B. H. Hamadani, C. a. Richter, D. J. Gundlach, R. J. Kline, I. McCulloch, M. Heeney, *J. Appl. Phys.* **2007**, *102*.
- [47] R. Noriega, J. Rivnay, K. Vandewal, F. P. V Koch, N. Stingelin, P. Smith, M. F. Toney, A. Salleo, *Nat. Mater.* **2013**, *12*, 1038.
- [48] T. Liu, A. Troisi, *Adv. Funct. Mater.* **2014**, *24*, 925.
- [49] S. V Novikov, D. H. Dunlap, V. M. Kenkre, P. E. Parris, a V Vannikov, *Phys. Rev. Lett.* **1998**, *81*, 4472.
- [50] Z. G. Yu, D. L. Smith, a Saxena, R. L. Martin, a R. Bishop, *Phys. Rev. Lett.* **2000**, *84*, 721.
- [51] M. Kemerink, T. Hallam, M. J. Lee, N. Zhao, M. Caironi, H. Sirringhaus, *Phys. Rev. B - Condens. Matter Mater. Phys.* **2009**, *80*, 1.
- [52] a. Salleo, T. W. Chen, a. R. Völkel, Y. Wu, P. Liu, B. S. Ong, R. a. Street, *Phys. Rev. B - Condens. Matter Mater. Phys.* **2004**, *70*, 1.
- [53] G. Horowitz, M. E. Hajlaoui, R. Hajlaoui, *J. Appl. Phys.* **2000**, *87*, 4456.
- [54] L. Mattias Andersson, W. Osikowicz, F. L. E. Jakobsson, M. Berggren, L. Lindgren, M. R. Andersson, O. Inganäs, *Org. Electron. physics, Mater. Appl.* **2008**, *9*, 569.
- [55] a. Salleo, R. a. Street, *Phys. Rev. B - Condens. Matter Mater. Phys.* **2004**, *70*, 1.
- [56] H. L. Gomes, P. Stallinga, M. Cölle, D. M. De Leeuw, F. Biscarini, *Appl. Phys. Lett.* **2006**, *88*, 150.
- [57] I. Mcculloch, M. Heeney, M. L. Chabinyc, D. Delongchamp, R. J. Kline, M. Cölle, W. Duffy, D. Fischer, D. Gundlach, B. Hamadani, R. Hamilton, L. Richter, A. Salleo, M. Shkunov, D. Sparrowe, S. Tierney, W. Zhang, *Adv. Mater.* **2009**, *21*, 1091.
- [58] B. Kang, M. Jang, Y. Chung, H. Kim, S. K. Kwak, J. H. Oh, K. Cho, *Nat. Commun.* **2014**, *5*, 4752.
- [59] S. J. Benight, C. Wang, J. B. H. Tok, Z. Bao, *Prog. Polym. Sci.* **2013**, *38*, 1961.